Graphical Analysis and Control of Cascaded H-bridge Multilevel Inverter Using Clarke Transformation with Neutral-Shift Strategy Under Non-Ideal Conditions

P. M. Lingom, *Member, IEEE*, Joseph Song-Manguelle, *Senior Member, IEEE*, Ideal O. Libouga, Mamadou L. Doumbia, *Member, IEEE*, Emmanuel Agamloh, Senior *Member, IEEE*

***Abstract*- This paper proposes a graphical approach using a 3D space vector representation to diagnose the unbalanced operation of a three-phase cascaded H-bridge (CHB) inverter operating under non-ideal conditions. Under ideal conditions, the application of the Clarke transformation to the inverter voltage phasor results in a circular trajectory within the stationary and orthogonal (αβ)-frame, enabling the inverter to supply balanced three-phase phase/line voltages and currents to the load. In contrast, when non-ideal conditions arise, such as DC voltage imbalances among the bridges or failed cells, the Clarke transformation of the inverter voltage phasor forms an elliptical path, leading to unbalanced operation. This paper discusses and highlights the characteristic differences between inverter-balanced and unbalanced operation modes. Additionally, a generalized neutral-shift method has been suggested to address unequal DC voltage sources simultaneously and failed cells without differentiation. The proposed control strategy ensures the inverter maintains balanced line-to-line voltages and currents, even when its phase voltages remain unbalanced. Simulation and experimental results from a three-cell (per phase) CHB inverter with a symmetrical RL load are provided to validate the effectiveness of the proposed approach. Finally, the study explores the impact of non-ideal conditions on modifying inverter voltage and current spectra.**

I. INTRODUCTION

In the last decades, the cascaded H-bridge multilevel inverter topology has become a solution for energy conversion in different industries [1], [2]. Its advantages, such as high efficiency, low harmonic distortion, modularity, and scalability, make it one of a promising technological power conversion in various high-power applications like renewable energy systems, electric vehicles, motor drives, and grid-connected systems [3-6], as illustrated in Fig. 1. Each H-bridge cell in a CHB inverter typically has its own isolated DC source (e.g., batteries, solar panels, supper-capacitor, or wind). However, the main challenge when using a three-phase CHB inverter is that it may exhibit unbalanced operation due to non-ideal conditions. In this paper, non-ideal conditions primarily refer to the scenario of unequal DC voltage inputs, where the connected DC sources exhibit different voltage levels across the H-bridge cells, leading to inverter output voltage waveforms.

In grid-connected photovoltaic (PV) inverter applications, the non-ideal condition results from inconsistent power generation among the power modules due to varying environmental factors, such as fluctuating solar irradiance,

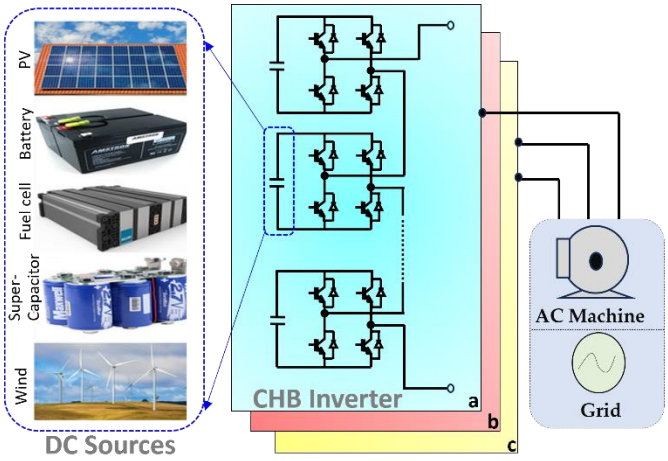

Fig. 1. The CHB inverter topology and its applications

partial shading, temperature inhomogeneity, and inconsistent degradation of some solar cells [7], [8]. In Electric vehicle (EV) and hybrid EV traction systems, battery degradation or unequal charging can cause imbalances in the DC-link voltage across H-bridge cells [9], [10], leading to unbalanced motor drive operation. Voltage imbalance at motor terminals can cause a current imbalance up to 6-10 times larger, leading to issues such as torque pulsation, vibrations, mechanical stress, lower efficiency, and motor overheating [11], [12].

Non-ideal conditions also occur when power electronic switches or associated gate driver boards in the power stage fail, leading to failure and bypass of H-bridge cells [13], [14]. When the H-bridge cell fails and is bypassed, it cannot contribute to the inverter output voltage, resulting in an unbalanced system operation.

Numerous studies have been conducted to develop effective control and modulation techniques suitable for CHB under non-ideal conditions (unequal DC source voltages and failed cells). Table 1 summarizes the most popular existing control strategies, highlighting their advantages and drawbacks. In [15], a neutral voltage modulation (NVM) strategy was proposed to address DC-link voltage inequality in CHBs. The conventional NVM method uses simple calculations to find the neutral voltage reference, incorporating zero-sequence voltage to compensate for output voltage imbalances and an offset voltage to extend the linear modulation range. However, the constraints on the neutral voltage are unclear, and in some cases, the maximum linear modulation index cannot be reached

Table 1. advantages and disadvantages of existing control scheme for CHB inverter under non-ideal conditions

CHB inverter with unequal DC-voltage sources	
Neutral Voltage Modulation (NVM) methods [15], [17], [18]	✓ Line-to-line voltage balancing capability. ✓ Simple implementation
	x Unsuitable for power balancing x Unsuitable under failed cell conditions
Zero-sequence Injection (ZSI) methods [8], [19], [20]	✓ Power balancing capability. ✓ Capable to operate in overmodulation Range
	x Unsuitable for line-to-line voltage balancing x Complex implementation ✓ Unsuitable under failed cell conditions
CHB inverter with failed cells	
Conventional Neutral-shift method [24]	✓ Line-to-line voltage balancing capability. ✓ Maxime the output voltage under faulty cells
	x Unsuitable under non-integer or dynamically changing DC voltage values x Unsuitable under severe failed cell conditions
Peak-reduction method [25]	✓ Line-to-line voltage balancing capability. ✓ Suitable under severe faulty cell conditions
	x Unsuitable under non-integer or dynamically changing DC voltage values x May cause overmodulation.

[16]. To address these limitations, an improved NVM method was introduced in [17], aimed at achieving a balanced three-phase output voltage in CHB inverters, even in the maximum modulation region, while minimizing overmodulation [18].

Zero-sequence voltage injection (ZSI) methods have proven effective for power control purposes under unequal DC voltage distribution conditions [8], [19], [20]. They maintain balanced three-phase currents under non-ideal conditions. However, the optimal zero-sequence injection method is considered the most advanced ZSI method, and it can only handle up to 20% of potential cell DC voltage inequality.

Several other studies have also proposed fault-tolerant control strategies for CHB inverter operation with faulty cells [21], [22]. These strategies can maintain balanced inverter output line voltages despite unbalanced phase voltages caused by failed cells [23], [24]. The two most commonly used techniques are the conventional neutral-shift and peak-reduction methods. Under the traditional neutral-shift methods, the inverter's neutral point is moved by adjusting the reference phase voltage angles [25]. In peak-reduction techniques, the neutral point is moved by adjusting the reference phase voltage magnitudes [26].

According to Table. 1, each investigated non-ideal condition has been addressed separately in the literature, utilizing an independent compensation control strategy. NVM and ZSI methods were developed for CHB systems under unequal DC voltage conditions and are inefficient for CHB systems with failed cells. Conversely, the conventional neutral-shift and peak-reduction methods are unsuitable for CHB inverters with DC voltage inequality, especially under non-integer or dynamically changing DC voltage levels. There is a gap in the literature regarding analysis and control methods that simultaneously address unequal DC voltage sources and failed cells in CHB topologies.

This paper proposes a unified approach utilizing graphical analysis to address the challenges posed by unequal DC voltage distribution and failed cells in CHB systems without differentiation. The proposed graphical analysis examines the unbalanced operation of the CHB inverter caused by non-integer DC voltage inputs, leading to a space vector diagram with non-integer entries. This novel graphical approach introduces a generalized control strategy based on the neutral-shift technique, which mitigates the effects of unequal DC voltage sources while simultaneously addressing cell failures. The proposed study applies to CHB-based power conversion inverter systems with DC source topologies, such as batteries, solar panels, supercapacitors, or wind energy systems, where maintaining equal DC voltage inputs is seldom feasible. Additionally, this method enhances the system's robustness and reliability, particularly in high-power variable frequency drive applications with multiple series-connected power cells, where some may fail and require bypassing.

II. A Space Vector Analysis of CHB Operation under Ideal Conditions

A. Analysis of inverter voltage states under ideal conditions

Let's assume the CHB topology (Fig. 1) that uses a k-series connected single-phase inverters (power cells), each supplied by an isolated DC voltage source noted $v_{dc,ij}$, where $i \in \mathbb{P} = \{a, b, c\}, j \in \mathbb{L} = \{1,2, \dots, k\}$, Under ideal operating conditions of the inverter, it is assumed that all DC voltage sources have equal values on all phase, $V_{dc,ij} = 1\,\text{p.u}$, such that:

- The output voltage of each H-bridge cell j on a given phase i is: $u_{ij} \in \mathbb{K} = \{-1, 0, 1\}$ p.u
- The number of voltage levels per phase is: $n = 2k + 1, n \in \mathbb{N}^*$ (an integer)
- The phase leg voltage amplitude is: $v_i = \sum_{j=1}^{k} u_{ij}$, $V_i \in \mathbb{N}^*$

Under these conditions, the three-phase CHB inverter produces a set of balanced three-phase line-to-neutral voltages It is a common accepted practice to convert the three-phase quantities of the inverter into its space-vector diagram to enable a more intuitive representation of the voltage states, making designing and optimizing its performance easier [27]. The analysis of the inverter output voltage phasor is performed in the stationary and orthogonal reference frame $\alpha\beta 0$ using the Clarke transformation as given in Eq (1).

$$v_i = [v_a\ v_b\ v_c]^T; v_{\alpha\beta 0} = [v_\alpha\ v_\beta\ v_0]^T \quad (1a)$$

$$v_{\alpha\beta 0} = M * v_i \quad (1b)$$

$$M = \sqrt{\frac{2}{3}} \begin{bmatrix} 1 & -1/2 & -1/2 \\ 0 & \sqrt{3}/2 & -\sqrt{3}/2 \\ 1/\sqrt{2} & 1/\sqrt{2} & 1/\sqrt{2} \end{bmatrix} \quad (1c)$$

Where, v_{abc} represents the line-to-neutral (LN) output voltage in abc the reference frame, while $v_{\alpha\beta 0}$ is the LN-voltage given the stationary orthogonal (complex) reference frame $\alpha\beta$.

For a balanced operation of a n-level inverter, the total number of output voltage states is given by n^3, which forms a cube surface in the $\alpha\beta 0$ -space. In the case of two-level inverters, there is only $2^3 = 8$ output voltage states exist, which correspond to the eight corners of the basic cube. The balanced operation of CHB multilevel inverter introduces additional intermediate states that are typically uniformly distributed between the limits of the basic cube. When applying the transformation described in Eq (1b) to a 7-level inverter with $k = 3$, the total number of inverter states is $7^3 = 343$, resulting in a regular cube surface as shown in Fig. 2(a). Fig. 2(b) illustrates the well-known space-vector hexagon associated with the 7-level inverter operation [27]. The solid lines in each sub-figure represent the theoretical limit of the inverter output voltage that can be produced under ideal operating conditions.

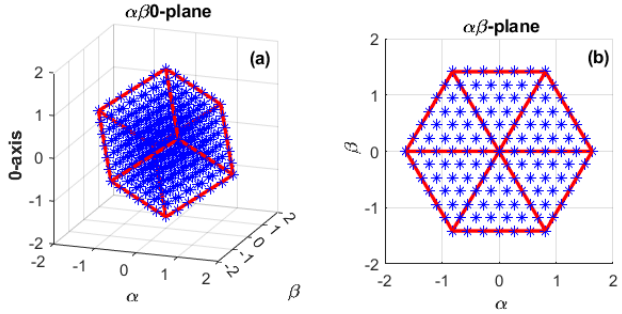

Fig. 2. Space vector representation of a balanced 7-level inverter output voltage states. 3D view and its projection in the $\alpha\beta -$ plane.

B. Analysis of CHB reference voltages under ideal conditions

In balanced operation, the PWM reference voltage signals can be expressed as:

$$v_i^{N*}(t) = m \cdot V_{\mathrm{dc}}\, sin\big(\omega_0 t - \theta_{o,i}\big) \tag{2}$$

with $\theta_{o,i} = (i-1)\frac{2\pi}{3}$ and $i \in \mathbb{K} = \{a = 1, b = 2, c = 3\}$

Where ω_0, m, and V_{dc} are the fundamental frequency, the modulation index, and the total inverter phase leg voltage, respectively. $\boldsymbol{N}$: represents the normal (balanced) operation under ideal conditions, specifically when the three-phase inverter has equal DC voltage sources with the same magnitude. A common-mode voltage is usually added to the PWM reference voltages to improve the utilization of the DC-source voltage. The modified PWM reference with the common-mode component injection is given by:

$$v_{0i}^{N*}(t) = v_i^{N*}(t) + v_0^*(t) \tag{3}$$

The injected common-mode voltage $v_0^*(t)$ can be the min-max voltage component (4) or the third harmonic component (5) where, V_0.is the magnitude of the fundament component of the LN voltage reference.

$$v_{0\mathrm{MM}}^*(t) = \frac{\min\limits_{i \in \boldsymbol{P}} v_{r,i}^*(t) + \max\limits_{i \in \boldsymbol{P}} v_{r,i}^*(t)}{2} \tag{4}$$

$$v_{0THI}^*(t) = \frac{V_0}{6}\sin\,(\omega_0 t) \tag{5}$$

The inverter PWM reference signal v_i^* is also Clarke transformed to $\alpha\beta 0$ reference frame as given in (6).

$$v_{i,\alpha\beta 0}^{N*} = M * [v_a^*\, v_b^*, v_0^*]^T \tag{6}$$

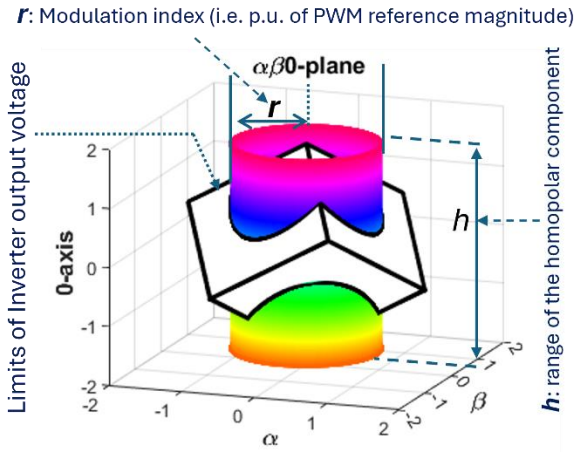

Fig. 3. Reference voltage cylinder and inverter output voltage cube surfaces.

The space vector representation of the PWM voltage reference vector in $\alpha\beta 0$-space when applied Eq (6) is shown in Fig. 3. This figure illustrates the coupled effects between inverter output voltage states and its PWM reference voltages. As shown in Fig. 3, the PWM reference voltage vector forms a cylindric shape in the $\alpha\beta 0$ -space. Because the homopolar component moves along the 0-axis, the family of all possible common-mode values corresponds to the cylinder height, which is centered and imbricated to the inverter voltage state cube surface. The inverter output-voltage cube is superposed to the reference-voltage cylinder within a maximum limit of $h \in [-\sqrt{3}, \sqrt{3}]$. The radius of the cylinder corresponds to the PWM modulation index.

For a balanced operation of the inverter, the PWM reference voltage must be maintained in its linear region. Subsequently, the reference-voltage cylinder surface should not exceed the limits of the inverter voltage cube surface as illustrated in Fig. 4(a). The edges of the intersected cylinder surface correspond to minimum (h_{min}) and maximum (h_{max}) values to be attained by all possible homopolar voltage components that can be added for an operation in the inverter linear region. The limits of the cylinder height under inverter linear region can be determined as follows:

$$h' = 2\sqrt{3} - \sqrt{2}\big(\max v_{r,i}^{\mathrm{N}*}(t) - \min v_{r,i}^{\mathrm{N}*}(t)\big) \tag{7}$$

From the $\alpha\beta$-plane shown in Fig. 4(b), the range of the PWM reference voltages corresponds to the area limited by circle shape. The radius of the largest circle inscribed on the regular hexagon gives the maximum output line-to-line achievable by the inverter. The reference voltage cylinder surface in Fig. 4(a) can be flattened into a two-dimensional graph as shown in Fig. 5, highlighting the possible common-mode paths at different

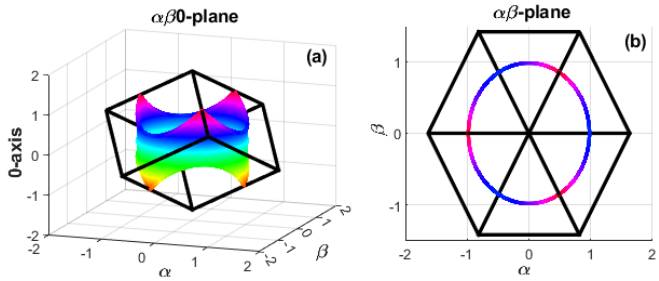

Fig. 4. Practical limits of the trajectory drawn by the PWM reference voltage vector for balanced and linear operation region.

modulation indexes. It is observed that the boundaries of the common-mode voltage components tend to reduce when the modulation index is increased. Fig. 6 shows a balanced operation of a 7-level inverter controlled by PWM method with a min-max voltage component injection at a modulation index of 1.1.

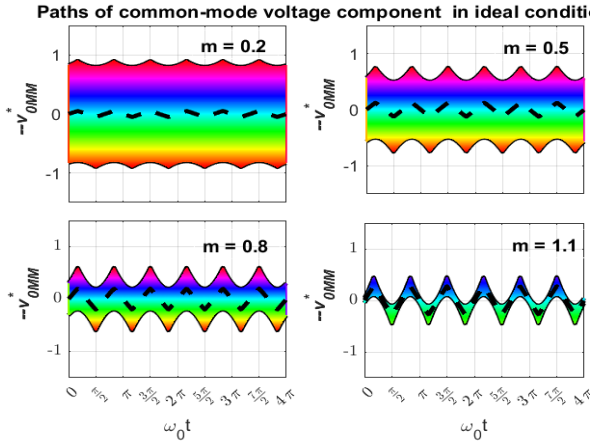

Fig. 5. Boundaries of common-mode voltage components for a CHB with $k = 3$ cells per-phase at different modulation indexes under ideal conditions.

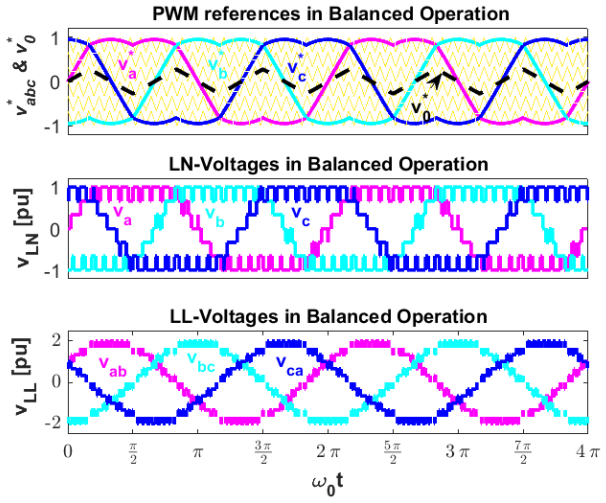

Fig. 6. Balanced operation of a 7-level CHB, $f_c/f_0 = 25$; $m = 1.1$.

III. A Space Vector Analysis of CHB Operation under Non-Ideal Conditions

A. *Analysis of inverter voltage states under non-ideal operating conditions*

Non-ideal operating condition of CHB refers to the scenario of unequal DC voltage condition [$0 < v_{dc,ij}(\text{p.u.}) < 1$] or the presence of one or more failed and bypassed cells [$v_{dc,ij}(\text{p.u.}) = 0$]. Under any of these operating conditions, the total phase leg voltage on the affected inverter phase reduces its nominal value. Fig.7 shows the space vector diagrams of inverter voltage states under selected unbalanced conditions summarized in Table 2. In this figure, the inverter output voltage states generated under balanced operation ($v_{dc,ij} = 1$) are shown with circles, whereas the actual voltage states under unbalanced conditions are shown in solid red dots for the failed power cells ($v_{dc,ij} = 0$), and in solid yellow dots for an operation with unequal DC voltage sources ($0<v_{dc,ij}<1$). By carefully analyzing Fig. 7, it can be observed that:

Table 2. Operation of a CHB with sample abnormal conditions.

	Cases	$v_{dc,a}$(p.u.)	$v_{dc,b}$(p.u.)	$v_{dc,c}$(p.u.)
Balanced condition	(a)	[1 1 1];	[1 1 1]	[1 1 1]
Operation with faulty cells	(b)	[1 1 1]	[1 1 0]	[1 1 1]
	(c)	[1 1 1]	[0 1 1]	[1 0 1]
Operation with unequal DC sources	(d)	[0.5 1 1]	[1 1 1]	[1 1 1]
	(e)	[1 1 1]	[0.8 1 0.2]	[1 1 1]
	(f)	[1 1 1]	[0.4 0.6 1]	[0.7 1 0]

- The amplitude of the inverter phase leg voltage $v_i = \sum_{j=1}^{k} v_{dc,ij}$ is a decimal number for unequal DC voltage source conditions, and the inverter voltage states won't vanish. They slightly move at all inside the boundaries of the box, as seen in Fig. 7(b).
- However, when there are failed power cells (i.e., when $v_i = \sum_{j=1}^{k} v_{dc,ij} \in N^*,, v_i$ is an integer), some voltage states are lost [Fig. 7(e) and (f)]. A similar behavior can be observed when the inverter is operating with significantly unequal DC-voltage source conditions [Fig. 7(b) and (c)].

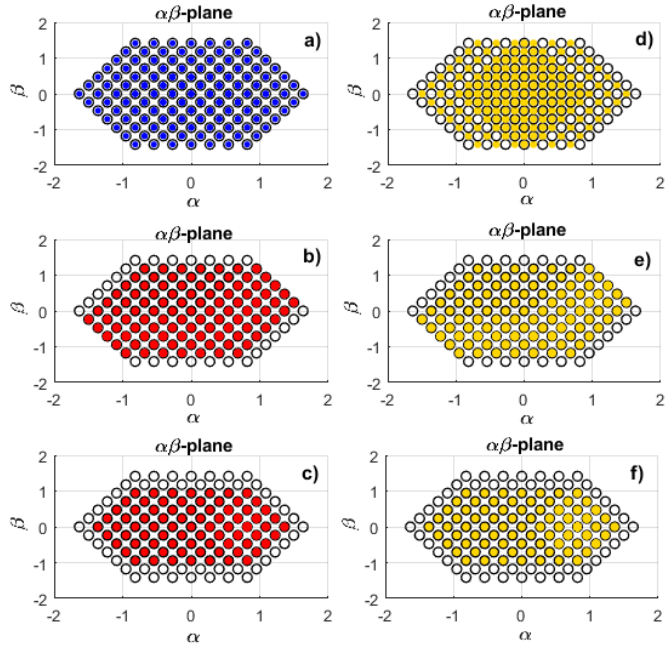

Fig. 7. Example of CHB space vector diagrams for different abnormal conditions.

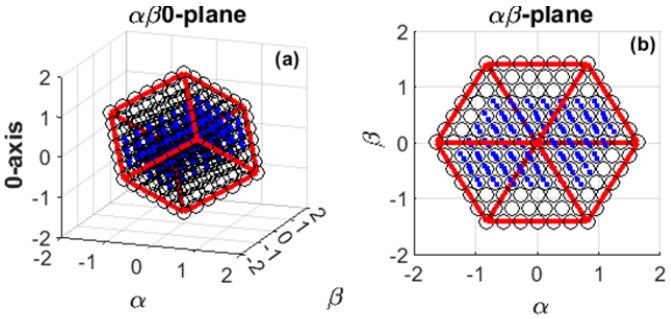

Fig. 8. Space vector representation of a CHB with k=3 cells under an unbalanced condition: $v_{dc,a} = [1\ 1\ 1]$; $v_{dc,b} = [1\ 0\ 0.2]$; $v_{dc,c} = [1\ 0.3\ 0.7]$.

Fig. 8 shows the space vector representation of inverter voltage states under non-ideal conditions, defined for $k = 3$ H-bridge cells per phase and voltage vectors supplied such that: $v_{dc,a} = [1\ 1\ 1]$, $v_{dc,b} = [0\ 0.2\ 1]$, and $v_{dc,c} = [0.7\ 1\ 0.3]$. As it can be seen, the inverter cannot produce all the possible voltage states under abnormal operating conditions, which affects the achievable limits of the inverter common-mode voltage quantities during the operation, as discussed in the next subsection.

B. *Analysis of PWM reference voltages under non-ideal conditions*

The analytical expression of the PWM reference voltage when the Clarke transformation is applied is given by:

$$\begin{bmatrix} v_{\alpha}^{F*}(t) \\ v_{\beta}^{F*}(t) \end{bmatrix} = \begin{bmatrix} A_{\alpha}^{F} cos\omega_0 t + B_{\alpha}^{F} cos\omega_0 t \\ A_{\beta}^{F} cos\omega_0 t + B_{\beta}^{F} cos\omega_0 t \end{bmatrix} \quad (8)$$

where $(A_{\alpha}^{N}, B_{\alpha}^{N})$, $(A_{\beta}^{N}, B_{\beta}^{N})$ are coefficients which depend on the available inverter phase leg voltage magnitude $V_{dc,i}$. $i \in \mathbb{P}$. They can be computed as shown in Eq (9):

$$A_{\alpha}^{F} = \frac{1}{3}\left(2V_{dc,a} + \frac{1}{2}V_{dc,b} + \frac{1}{2}V_{dc,c}\right) \quad (9a)$$

$$B_{\alpha}^{F} = -\frac{1}{2\sqrt{3}}\left(V_{dc,b} - V_{dc,c}\right) \quad (9b)$$

$$A_{\beta}^{F} = -\frac{1}{2\sqrt{3}}\left(V_{dc,b} - V_{dc,c}\right) \quad (9c)$$

$$B_{\beta}^{F} = \frac{1}{2}\left(V_{dc,b} + V_{dc,c}\right) \quad (9d)$$

In balanced operating conditions, $V_{DC,a} = V_{DC,b} = V_{DC,c} = V_{dc} = \sum_{j=1}^{k} V_{dc,ij}$. This is not true under unbalanced operation condition, where $V_{DC,a} \neq V_{DC,b} \neq V_{DC,c}$. In this case, the trajectory of the PWM reference vector describes an elliptic path in the $\alpha\beta$ −plane. Table 3 presents sample unbalanced cases for a 7-level CHB under failed cells and unequal DC sources to analyze the behavior of its reference voltage phasor as discussed in Fig. 9. The red and blue lines represent the trajectory of the reference voltage vector under balanced and unbalanced conditions, respectively. It is observed that, under certain unbalanced conditions, the inverter reference voltage vector forms an ellipse path that may have horizontal [Fig. 9(a)] or vertical [Fig. 9(b)] orientations. The trajectory of the inverter reference voltage phasor can also draw an ellipse with a different inclination angle in other unbalanced conditions as illustrated in [Fig. 9(c)-(d)]. Once this mechanism is understood, it can be predicted that the inverter loses rotational symmetry under unbalanced conditions, resulting in unbalanced output voltages and currents if its PWM reference voltage signals are not appropriately adjusted.

Fig. 10 presents a space vector representation of the output voltage states and PWM reference voltages for an inverter with $k = 3$ cells per phase operating under a specific unbalanced condition ($v_{dc,a} = [1\ 1\ 1]$; $v_{dc,b} = [1\ 0\ 0.2]$; $v_{dc,c} = [1\ 0.3\ 0.7]$). The boundaries of all possible common-mode voltage components in function of the achievable limits of the inverter output voltages are highlighted.

Table 3. Example of non-ideal conditions of a 7-level CHBI with $k = 3$ cells

Cases	$v_{dc,a}$(p.u.)	$v_{dc,b}$(p.u.)	$v_{dc,c}$(p.u.)
(a)	[1 1 0.8]	[0.6 1 0.5]	[0.6 1 0.5]
(b)	[0.4 0 1]	[1 1 0.7]	[1 1 0.7]
(c)	[1 1 1]	[1 1 1]	[0.5 0.4 1]
(d)	[1 0.5 1]	[0.5 0.5 0.3]	[0.5 1 1]

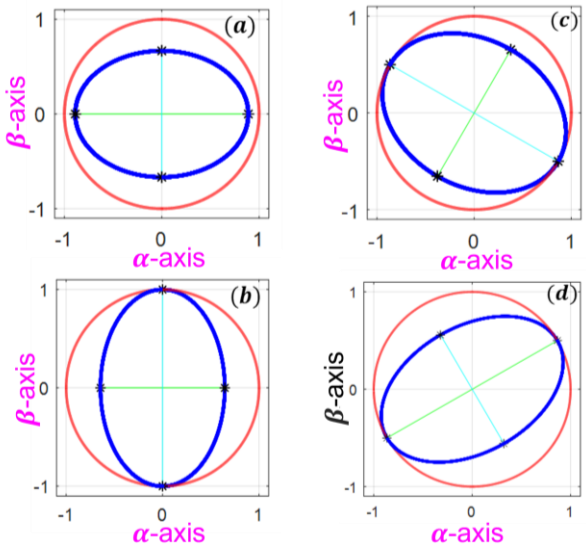

Fig. 9. Behavior of the PWM reference voltage vector for a CHB with k = 3 power cells per phase under non-ideal conditions.

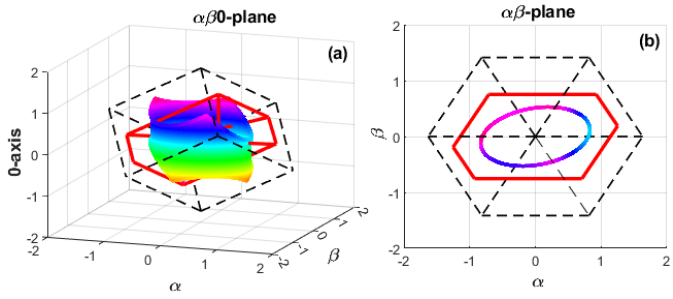

Fig. 10. Modified cube and cylinder surfaces for a CHB with k=3 cells under an unbalanced condition: $v_{dc,a} = [1\ 1\ 1]$; $v_{dc,b} = [1\ 0\ 0.2]$; $v_{dc,c} = [1\ 0.3\ 0.7]$.

It is shown that, the inverter-output voltage limits have been decreased from their nominal values under this abnormal condition. The unbalanced operation of the inverter can be easily perceived from the elliptical shape of its voltage phasor in the $\alpha\beta$-plane as shown in [Fig. 10(b)]. The altered PWM reference voltage cylinder surface vector in Fig. 10(a) can be flattened to a two-dimensional graph, and the new limits of all the common-mode voltage components are shown in Fig. 11. It is shown that the possibility of injecting an appropriate homopolar voltage component to adjust the behavior of the inverter's differential-mode quantities.

Adding an appropriate common-mode voltage to the inverter reference voltages influences the current flow into the inverter's phase, maintaining balanced three-phase inverter output currents under unbalanced conditions [20], [28], but the zero-sequence injection-based control methods may not be sufficient to provide proper compensation in terms of maintaining balanced line-to-line voltages to the load. Fig. 12 shows the LN-voltage and LL-voltage waveforms for a CHB with $k = 3$ cells per phase operating under an abnormal condition ($v_{dc,a} = [1\ 1\ 1]$; $v_{dc,b} = [1\ 0\ 0.2]$; $v_{dc,c} = [1\ 0.3\ 0.7]$). As can be seen, the inverter phase and line voltages remain unbalanced because no compensation control technique has been applied during the operation process. The following section suggests a compensation control method for CHB operation under non-ideal conditions. The proposed control method involves moving the inverter floating neutral point by adjusting the inverter phase voltage angles to balance output

currents and maximize the utilization of remaining operative HB cells under a given non-ideal condition.

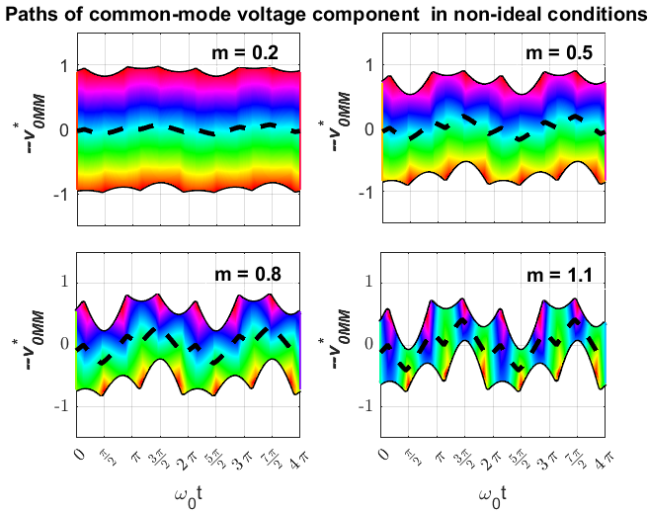

Fig. 11. Boundaries of common-mode voltage components for a CHB with $k = 3$ cells at different modulation indexes under a non-ideal condition.

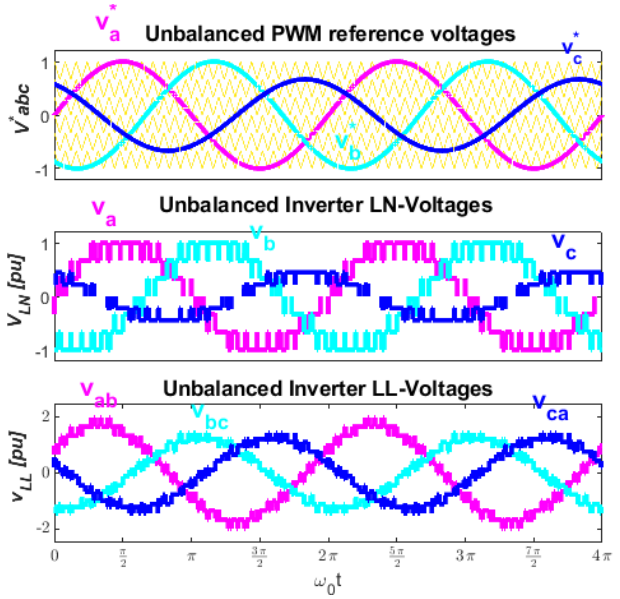

Fig. 12. An Operation of a CHB with $k = 3$ cells per phase under a non-ideal condition ($v_{dc,a} = [1\ 1\ 1]$; $v_{dc,b} = [1\ 0\ 0.2]$; $v_{dc,c} = [1\ 0.3\ 0.7]$).

IV. A Generalized Neutral-shift Strategy suitable for CHB Operation under Non-Ideal Conditions

The proposed generalized neutral-shift method assumed that the phase angles between a and b or c are no longer $2\pi/3$, and the inverter reference voltages can be expressed as given in Eq. (10):

$$\begin{cases} v_a^*(t) = V_{dc,a}\cos(\omega_0 t) \\ v_b^*(t) = V_{dc,b}\cos(\omega_0 t - \theta_{ab}) \\ v_c^*(t) = V_{dc,c}\cos(\omega_0 t - \theta_{ca}) \end{cases} \quad (10)$$

The analytical expression of the corrected PWM reference voltage when applied the Clarke transformation is given in Eq. (11). The parameters A_α^C, B_α^C, A_β^C, B_β^C, A_0^C, and B_0^C of the PWM reference voltage phasor under these circumstances can be determined by:

$$\begin{bmatrix} v_\alpha^{C*}(t) \\ v_\beta^{C*}(t) \\ v_0^{C*}(t) \end{bmatrix} = \begin{bmatrix} A_\alpha^C cos\omega_0 t + B_\alpha^C cos\omega_0 t \\ A_\beta^C cos\omega_0 t + B_\beta^C cos\omega_0 t \\ A_0^C cos\omega_0 t + B_0^C cos\omega_0 t \end{bmatrix} \quad (11)$$

$$A_\alpha^C = \frac{1}{3}\left(2V_{dc,a} - \frac{1}{2}V_{dc,b}\cos\theta_{ab} - \frac{1}{2}V_{dc,c}\cos\theta_{ca}\right) \quad (12a)$$

$$B_\alpha^C = -\frac{1}{3}\left(V_{dc,b}\sin\theta_{ab} - V_{dc,c}\sin\theta_{ca}\right) \quad (12b)$$

$$A_\beta^C = -\frac{\sqrt{3}}{3}\left(V_{dc,b}\cos\theta_{ab} - V_{dc,c}\cos\theta_{ca}\right) \quad (12c)$$

$$B_\beta^C = \frac{1}{2}\left(V_{dc,b}\sin\theta_{ab} + V_{dc,c}\sin\theta_{ca}\right) \quad (12d)$$

The parametric ellipse equation in the $\alpha\beta$-plan defined by the PWM reference voltage vector under unbalanced conditions can be expressed as shown in Eq. (13).

$$Px^2 + Qxy + Sy^2 + T = 0 \quad (13)$$

$$P = \left(A_\beta^C\right)^2 + \left(B_\beta^C\right)^2;\ Q = -2\left(A_\alpha^C A_\beta^C + B_\alpha^C B_\beta^C\right) \quad (14)$$

$$S = (A_\alpha^C)^2 + (B_\alpha^C)^2;\ T = -\left(A_\alpha^C B_\beta^C - A_\beta^C B_\alpha^C\right)^2 \quad (15)$$

If $Q \neq 0$, the general ellipse equation can be written as follows.

$$\frac{\left[(x-C_x)\cos\theta + (y-C_y)\sin\theta\right]^2}{R_x^2} + \frac{\left[(x-C_x)\sin\theta + (y-C_y)\cos\theta\right]^2}{R_y^2} \quad (16)$$

Where R_x, R_y, and θ stand for the major-axis, minor-axis, and the tilt angle of the ellipse (blue line) respectively, and they are highlighted in Fig. 13. The coordinates (C_x, C_y) is the center of the ellipse, and its tilt angle θ can be determined by the following relationship:

$$tan\,\theta = \frac{2Q}{P-S} \quad (17)$$

The fundamental the proposed neutral-shift control relies on finding the new achievable circle from the ellipse equation generated by the inverter PWM reference voltages in the $\alpha\beta$ −plane under unbalanced conditions. This is achieved by establishing appropriate criteria that transforms the ellipse equation into a circle equation. The new circle equation (18b) of the corrected PWM reference voltage can be obtained by fulfilling the condition given in Eq. (18a). Fig.13 illustrates how an inverter PWM reference ellipse shape is transformed into a circle shape (green line) when applying the proposed neutral-shift strategy.

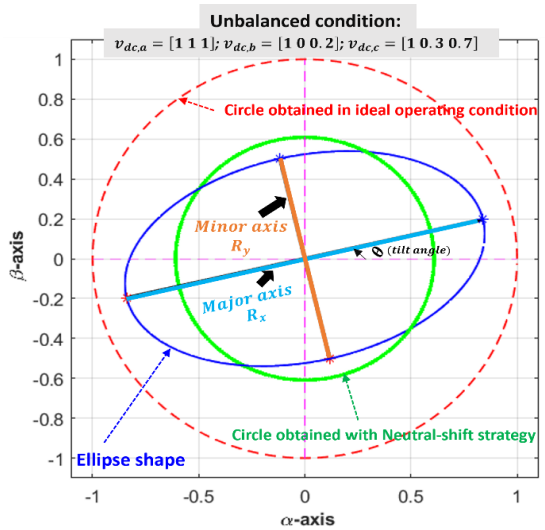

Fig. 13. . Transformation of an inverter PWM reference ellipse shape into a circle shape using the proposed neutral-shift strategy.

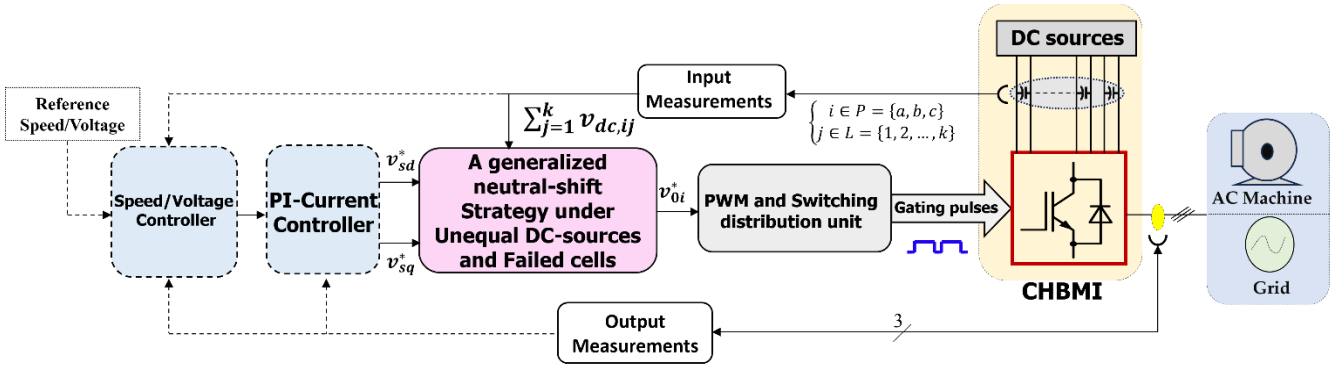

Fig. 14. The block diagram of the feedback control scheme with the suggested generalized neutral-shift strategy.

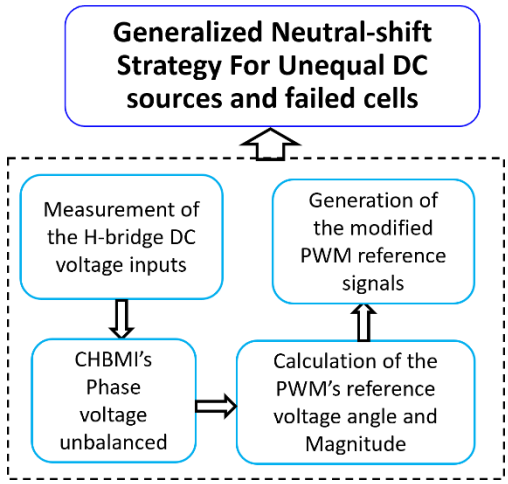

Fig. 15. Implementation steps of the suggested neutral-shift strategy.

$$\begin{cases} Q = 0 \\ S = P \end{cases} \tag{18a}$$

$$\frac{S}{T}x^2 + \frac{P}{T}y^2 = 1 \tag{18b}$$

The corrected PWM reference voltages are designed to neutralize the effects of unbalanced LN voltages, making it possible to achieve balanced output LL voltages at any non-ideal conditions.

Fig.14 shows the block diagram of the overall feedback control scheme with the suggested generalized neutral strategy. The first stage of this scheme is the outer control loop, which varies based on the application. For instance, in motor drive applications, it regulates the speed/torque of the electrical machine. In PV-based or battery-based energy conversion systems, it regulates the sum of the DC-link voltages to determine the overall active power P required to control the system. The outer voltage controller loop indirectly gives the active power reference in the form of d-axis current reference. The q-axis current reference is chosen depending on the system requirements, typically set to zero to inject the energy into the grid with a unity power factor. dq-currents are also regulated by a proportional-integral (PI) controller, which delivers the inverter reference voltage in the synchronous frame, which are transformed back to the three-phase coordinates in stage 3, where the suggested neutral-shift strategy (Fig. 15) under non-ideal conditions is applied. In Stage 3, inverter voltage reference angles and magnitudes are adequately adjusted using g the neutral shift strategy under unequal DC voltages or failed cells. Finally, a PD-PWM method in stage 4 is used to generate gating signals to control the power switches.

Fig. 16 depicts inverter voltage waveforms of an inverter with $k = 3$ cells per-phase ($v_{dc,a} = [1\ 1\ 1]$; $v_{dc,b} = [1\ 1\ 1]$; $v_{dc,c} = [1\ 0.4\ 0.6]$) and controlled by the suggested neutral-shift method. It is clearly observed that, the inverter phase voltages are remained unbalanced, however the inverter line voltages have been successfully rebalanced by properly adjusting its PWM reference phase voltages using the neutral-shift strategy. The min-max voltage component is injected to extend the inverter modulator linear region under unbalanced conditions.

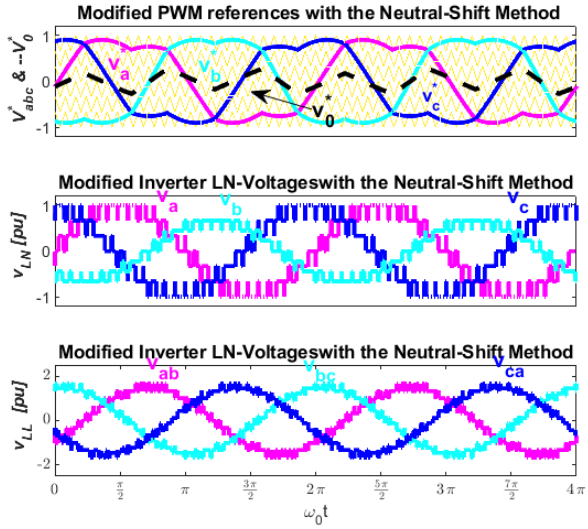

Fig. 16. Voltage waveforms for a CHB with $k = 3$ cells per phase operating under corrected mode using the neutral-shift control strategy.

V. Experimental Validation and Test Results

A. Experimental Setup description

This section discusses steady-state experimental results obtained from a scaled-down laboratory test bench equipped with $k = 3$ AC-DC-AC Semikron SK 10GD12T4ET power modules. The three-phase 7-level inverter is connected to a Y-connected R-L load, switching each phase leg at 1 kHz. The 15-ohm resistance balances the lab's system setup performance and experimental constraints, such as the inverter's power source's voltage and current ratings. This value was selected to ensure the safe operation and repeatability of the experiments at lower current ratings under various DC voltage conditions and cell failures. The proposed compensation neutral-shift control strategy is implemented and executed on Simulink real-time target PC using a NI-PCI 6229 board to redirect the appropriate PWM command signals to the inverter gate drives.

The unequal DC-voltage conditions for the inverter were performed by feeding each inverter H-bridge cell through a DC-power supply, model NES-1000-80 (0 to 80 V). A bypassed contactor is connected at the output of an individual H-bridge cell and is used to emulate the system operation with one or more faulty cells. The overall experimental system picture is depicted in Fig. 17, and its key parameters are summarized in Table 4. Several abnormal operating conditions were tested to emulate the inverter's unbalanced operation with unequal DC-voltage and fail cell conditions. The following selected abnormal conditions summarized in Table 5 are presented and discussed for simplicity.

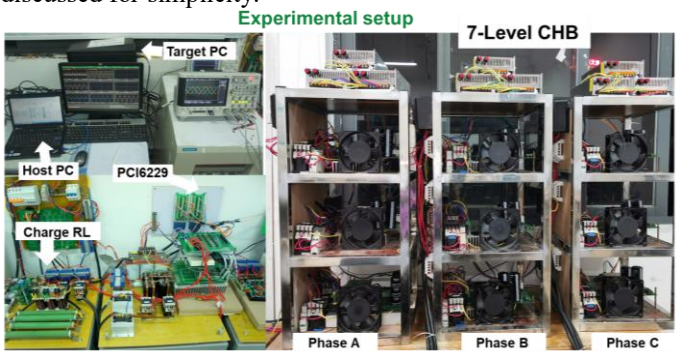

Fig. 17. Picture of the scaled-down laboratory prototype

Table 4. Key parameters of the experimental system.

No	Devices	Characteristics
1	IGBT	Semikron SK 10GD12T4ET 1200 V/15 A
2	DC Link capacitors	Photo Flash 3600μF, 450V/360w
3	DC-power supply	NES-1000-80 rated at 80 V, 12.5 A.
4	Gate drives	Semikron SKHI 61. R
5	Voltage sensors	model CHV-100/800.
6	Current sensors	TKC50BR 4.0V/50A
8	Resistive load	15 Ω
9	Line reactor	TLDKQ 8A/30mH
10	Data acquisition board	Dual NI-DAQ PCI 6229
11	Oscilloscope	Tektronix MD04104C

Table 5. Selected tested abnormal operating conditions.

Cases	$v_{dc,a}$(V)	$v_{dc,b}$(V)	$v_{dc,c}$(V)
(1)	$50 * [0\ 1\ 1]$	$50 * [1\ 1\ 1]$	$50 * [1\ 1\ 1]$
(2)	$50 * [0.6\ 1\ 0.4]$	$50 * [1\ 1\ 1]$	$50 * [1\ 1\ 0]$
(3)	$50 * [1\ 1\ 1]$	$50 * [1\ 1\ 1]$	$50 * [0.8\ 0\ 0.2]$

B. Test results and Discussion.

1. Steady-state time-domain experimental results

Figs 18-20 show the corresponding experimental results of each unbalanced operating condition in Table 5. In each figure, both inverter voltage and current waveforms obtained under abnormal [Figs 18(a)-20(a)] and corrected [Figs 18(b)-20(b)] modes waveform. In Fig. 18 (case 1), the three-phase system imbalance is only caused by a bypassed cell (cell#1) in phase *A*. Fig. 19 (case 2) shows, a bypassed cell in phase *A*, while all the H-bridge cells in phase *C* are fed with different DC-voltage values. Finally, in Fig. 20 (Case 4), the imbalance of the three-phase system results from two scenarios: a bypass cell in inverter phase *C* and its remaining operational H-bridge cells are supplied by different DC-voltage magnitudes. Figs 18(a)-20(a) indicate the unbalanced state of the inverter output voltage and current waveforms when no compensation control method applied during abnormal conditions. However, in corrected inverter operation mode, the proposed neutral-shift compensation control technique, which has modified the inverter PWM reference voltage amplitudes and angles, is used to keep the balanced inverter LL-voltages, even if the inverter LN-voltage remains unbalanced, as shown in Figs 18(b)-20(b) The three-phase inverter output currents for each abnormal case have been successfully re-balanced in corrected mode.

C. Analysis of inverter experimental data using Clarke Transformation

This section discusses the space vector diagrams of voltage and current and the associated spectra of experimental data to validate the correctness of the proposed analysis approach using the Clarke transformation.

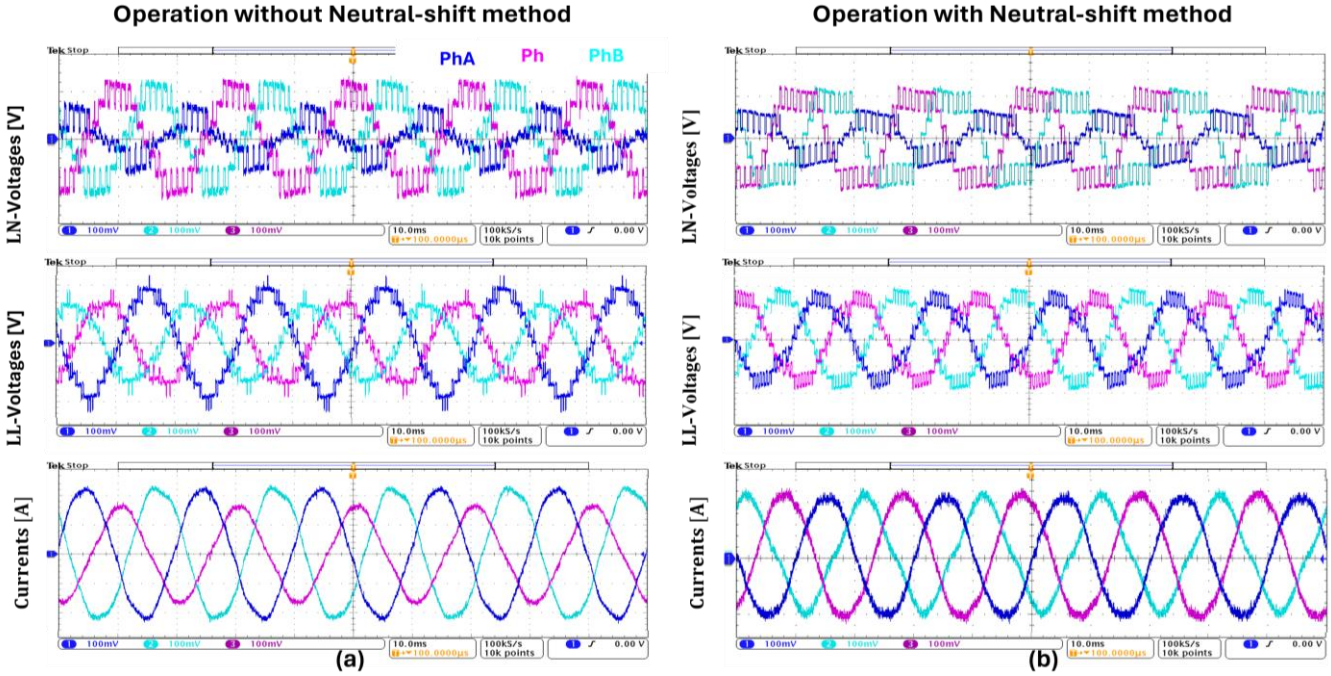

Fig. 18. Voltage and current test results for a CHB with $k = 3$ cells per phase under operating condition case 1: $v_{dc,a} = [0\ 50\ 50]$ V; $v_{dc,b} = [50\ 50\ 50]$ V; $v_{dc,c} = [50\ 50\ 50]$ V: (a) Operation without the proposed neutral-shift method; (b) Operation with the proposed neutral-shift method.

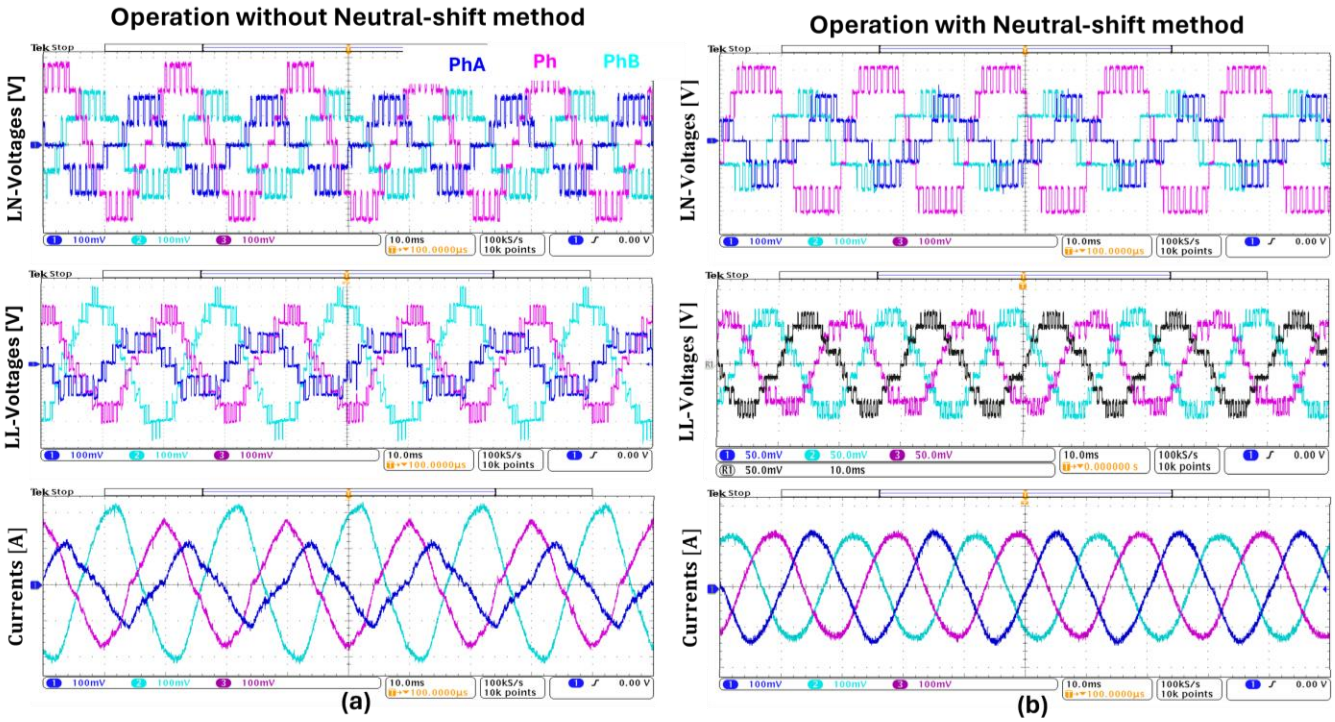

Fig. 19. Voltage and current test results for a CHB with $k = 3$ cells per phase under operating condition case 2: $v_{dc,a} = [\,20\ 50\ 30]$V; $v_{dc,b} = [50\ 50\ 50]$V; $v_{dc,c} = [50\ 50\ 0]$V: (a) Operation without the proposed neutral-shift method; (b) Operation with the proposed neutral-shift method.

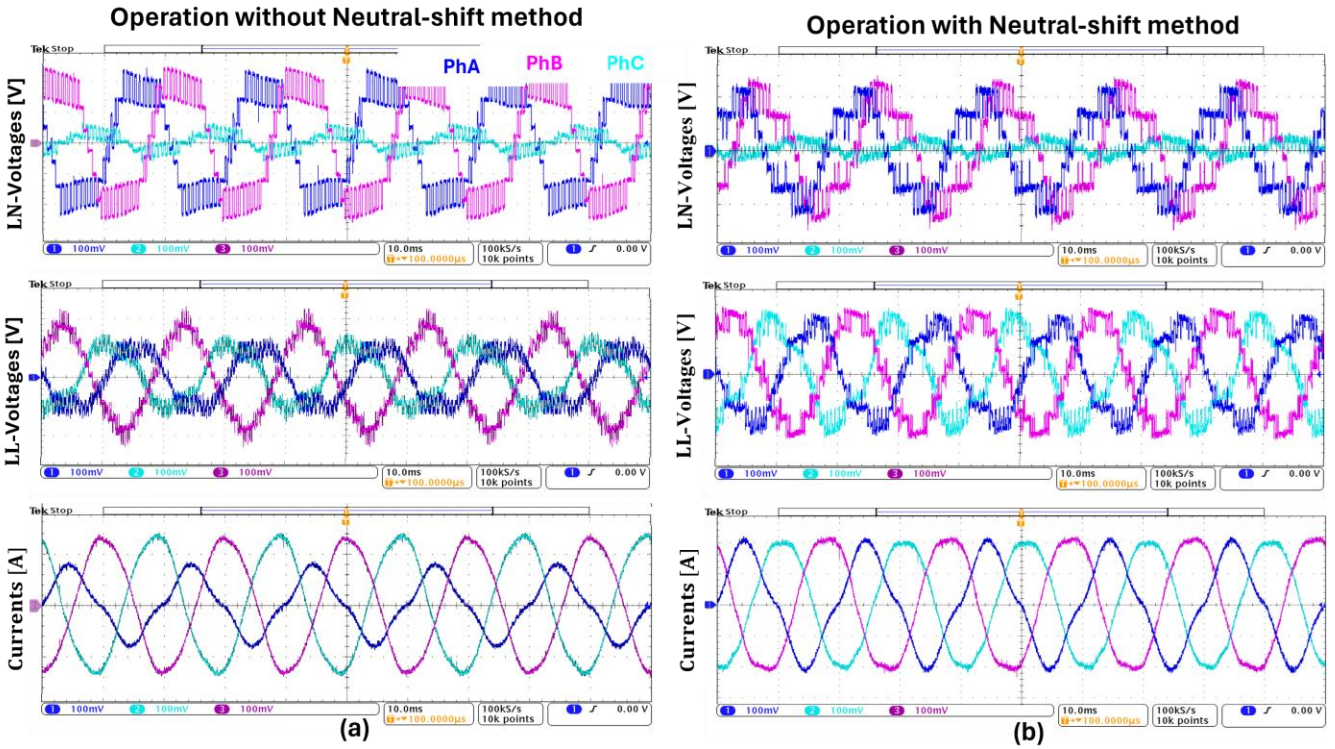

Fig. 20. Voltage and current test results for a CHB with $k = 3$ cells per phase under operating condition case 3: $v_{dc,a} = [50\ 50\ 50]$V; $v_{dc,b} = [50\ 50\ 50]$V; $v_{dc,c} = [40\ 0\ 10]$V: (a) Operation without the proposed neutral-shift method; (b) Operation with the proposed neutral-shift method.

The experimental waveforms (Fig. 18) were saved as text files and later imported into MATLAB for further analysis. We then applied the Clark transformation to the data in both the time and frequency domains. Figs. 22 and 23 display the results of the transformation both before and after processing. Before, Fig. 21 shows the inverter phase voltage, current space vector diagrams, and their respective spectra in $\alpha\beta$ -plane under ideal conditions ($v_{dc,a} = [50\ 50\ 50]$ V ; $v_{dc,b} = [50\ 50\ 50]$ V; $v_{dc,c} = [50\ 50\ 50]$ V). It can be observed that the inverter current Clark's vector pattern for

balanced operation is a perfect circle. From the harmonic point of view, the inverter voltage and current spectra do not contain carrier band and triple baseband harmonics in the $\alpha\beta$-plane. They are canceled by differentiating inverter phase voltage/current using the Clarke transformation. This is not valid under an unbalanced operation caused by non-ideal conditions, as shown in Fig. 22.

The experimental case studied in Fig. 22 is similar to the one discussed in Fig. 18 ($v_{dc,a} = [0\ 50\ 50]$ V ; $v_{dc,b} = [50\ 50\ 50]$ V; $v_{dc,c} = [50\ 50\ 50]$ V). As can be observed, the output current phasor has an elliptical shape, indicating the inverter's unbalanced operation, which leads to more harmonic distortions than under ideal operation. The spectrum of the inverter voltage phasor in Fig. 22 contains two relevant harmonic components with high magnitude. The first is a triplen baseband harmonic component at the frequency of 150Hz ($3 \cdot f_0$), while the second is a carrier-band harmonic component at the frequency of 1000Hz (f_c). It is evident that compared to ideal operation (Fig. 19), these unwanted components are no longer common-mode harmonics in a faulty condition. Therefore, they weren't canceled out through the differentiation of the inverter phase voltage using the Clarke transformation in $\alpha\beta$-plane.

Fig. 23 depicts the voltage and current phasor as well as their spectra under the unbalanced operation of the inverter when controlled by the proposed neutral-shift method. The voltage phasor for unbalanced operation without the neutral-shift method (Fig. 22) differs from the one when using the neutral shift, as shown in Fig. 23.

This adjustment successfully rebalanced inverter line voltages and currents and modified the inverter phasor shapes in the $\alpha\beta$-plane. As a result, the rebalanced three-phase inverter output forms a circular shape in the ab-plane even if its phase voltage remains unbalanced. However, from the harmonic analysis point of view, the suggested neutral-shift method hasn't eliminated some undesirable harmonic content, such as triple baseband harmonic component at the frequency of 150Hz ($3 \cdot f_0$).

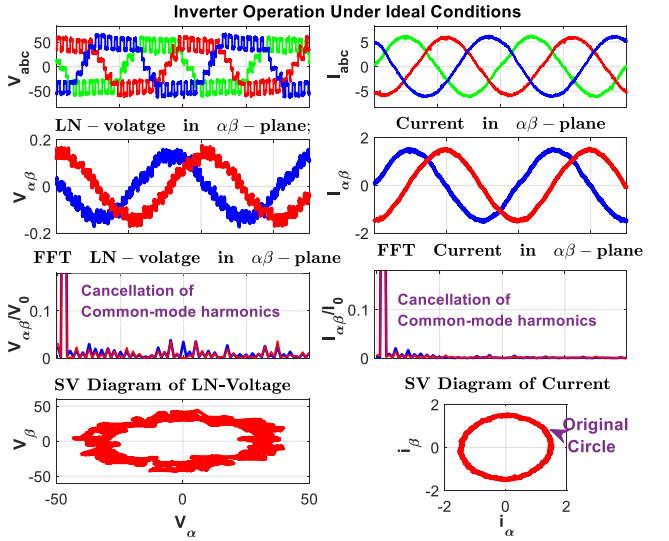

Fig. 21. Inverter voltage and current phasor and their spectra under a balanced operation: ($v_{dc,a} = [50\ 50\ 50]$; $v_{dc,b} = [50\ 50\ 50]$; $v_{dc,c} = [50\ 50\ 50]$).

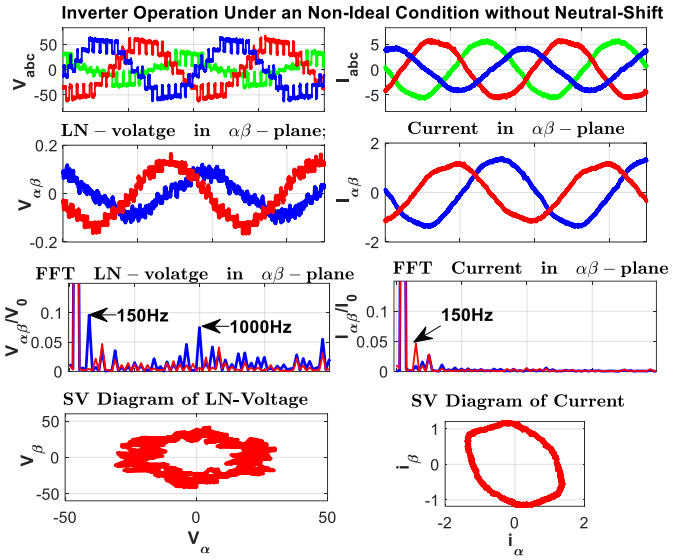

Fig. 22. Inverter voltage and current phasor and their spectra under an unbalanced operation ($v_{dc,a} = [0\ 50\ 50]$; $v_{dc,b} = [50\ 50\ 50]$; $v_{dc,c} = [50\ 50\ 50]$) without the neutral-shift method.

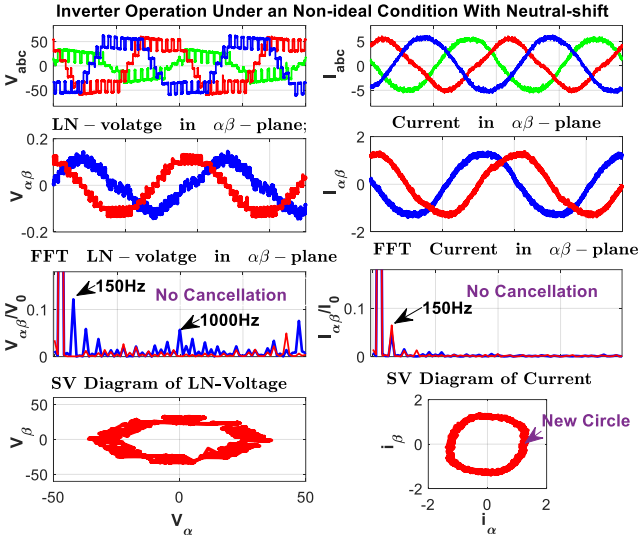

Fig. 23. Inverter voltage and current phasor and their spectra under an unbalanced operation ($v_{dc,a} = [0\ 50\ 50]$V ; $v_{dc,b} = [50\ 50\ 50]$ V ; $v_{dc,c} = [50\ 50\ 50]$V) with the neutral-shift method.

This limitation can be addressed by optimizing the switching strategy of the proposed neutral-shift strategy to mitigate some classes of harmonics during the compensation control process of the inverter's unbalanced operation, as discussed in [11].

VI. CONCLUSION

This paper has proposed a graphical analysis of the interaction between cascaded H-bridge inverter output voltage states and its PWM reference voltage using Clarke transformation under non-ideal conditions, such as faulty cells, DC-source failure, and unequal DC voltages. The Clarke transform matrix was used to convert the inverter's three-phase quantities to differential-mode and common-mode quantities to better understand its output voltage and current phasor shapes under non-ideal operating conditions. The proposed study is

also crucial in identifying the linear region boundaries of all potential common-mode voltage components that can be injected under non-ideal conditions. Understanding this mechanism makes finding an appropriate homopolar component to maintain balanced inverter output currents under non-ideal conditions more straightforward. A generalized neutral-shift strategy was also proposed to produce balanced inverter line voltages and currents under non-ideal conditions. The effectiveness of the suggested control strategy was proven through experiments conducted on a laboratory prototype based on a 3-cell per-phase cascaded H-bridge inverter. Finally, an analysis of the experimental inverter output voltage and current data and their respective spectra in $\alpha\beta$-plane was conducted to validate the relevance of the suggested study. The readjusting of the inverter voltage reference phase voltage angles and amplitudes through the suggested control scheme redistributes the ON and OFF times, directly impacting the inverter's switching and conduction losses. Future work will investigate these aspects in detail, assessing how the proposed method influences the energy distribution among modules and quantifying its effects on the inverter power losses and efficiency.

REFERENCE

[1] A. Salem, H. V. Khang, K. G. Robbersmyr, M. Norambuena and J. Rodriguez, "Voltage source multilevel inverters with reduced device count: Topological review and novel comparative factors," *IEEE Trans. Power Electron*. vol. 36, pp. 2720–2747, 2021.

[2] S. Rahman et al, "A Combinational Level-Shifted and Phase-Shifted PWM Technique for Symmetrical Power Distribution in CHB Inverters," *IEEE J. Emerg. Sel. Top. Power Electron*., vol. 11, no. 1, pp. 932–941, Feb. 2023.

[3] Hussein Mahdi, Bjarte Hoff, Trond strem, "A Review of Power Converters for Ships Electrification," *IEEE Trans. Power Electron*. vol.38, no.4, pp.4680-4697, 2023.

[4] J. Song-Manguelle, T. Thurnherr, S. Schröder, A. Rufer, and J.-M. Nyobe-Yome, "Re-generative asymmetrical multi-level converter for multimegawatt variable speed drives," in Proc. IEEE Energy Convers. Congr. Expo., 2010, pp. 3683–3690.

[5] J. Tian, et al, "Individual DC voltage balance control for cascaded H-bridge electronic power transformer with separated DC-link topology," *IEEE Access*, 2019, 7, 38558–38567.

[6] A. M. Rauf, M. Abdel-Monem, G. O. Hegazy, "A Review on Multilevel Converters for Efficient Integration of Battery Systems in Stationary Applications," *Energies*., 2023, vol. 16, no. 10, pp.4133; https://doi.org/10.3390/en16104133.

[7] M. Meraj et al, "Novel Level Shifted PWM Technique for Unequal and Equal Power Sharing in Quasi Z-Source Cascaded Multilevel Inverter for PV Systems," *IEEE J. Emerg. Sel. Top. Power Electron*., vol. 11, no. 4, pp. 932–941, Aug. 2023

[8] S. Rivera, S. Kouro, B. Wu, J. Leon, J. Rodriguez, and L. Franquelo, "Cascaded H-bridge multilevel converter multistring topology for large scale photovoltaic system," in *Proc. IEEE Int. Symp. Ind. Electron.*, Jun. 2011, pp. 1837–1844.

[9] J. Lamb, and B. Mirafzal, "An Adaptive SPWM Technique for Cascaded Multilevel Converters with Time-Variant DC Sources," *IEEE Trans. Ind. Appl.*, 2016, 52, 4146–4156.

[10] J. Xiong, F. Zhou, Q. Li, "Soft-switching modulation of the multilevel cascaded H-bridge inverter under DC source fault," *IET Gen, Trans & Dist.*, 2021, https://doi.org/10.1049/gtd2.12105.

[11] P. M. Lingom, et al, "VFD-Induced Torsional Stresses in Pumped Hydropower Storage Applications," *IEEE Access*., vol. 12, no. pp. 35984-360012024, 2024.

[12] Submersible Pump Engineering, "Unbalanced currents and submersible motors," *SMENG*, 2002, 1–2.

[13] S. P. Gautam, M. Jalhotra, L. K. Sahu, M. R. Kumar, and K. K. Gupta, "A Survey on Fault Tolerant and Diagnostic Techniques of Multilevel Inverter," *IEEE Access*, vol. 11, pp. 608666–60888, 2023.

[14] I. Marzo, A. Sanchez-Ruiz, J. A. Barrena, G. Abad, and I. Muguruza, "Power Balancing in Cascaded H-Bridge and Modular Multilevel Converters Under Unbalanced Operation: A Review," *IEEE access*, vol. 9, 110525-110543, 2021.

[15] Y. Cho, T. Labella, J. S. Lai, and M. K. Senesky, "A carrier-based neutral voltage modulation strategy for multilevel cascaded inverters under unbalanced DC sources," *IEEE Trans. Ind. Electron*., 2014, vol. 61, no. 2, pp. 625–636, 2014.

[16] Z. B. Ye, and T. T. Wang, "A PWM strategy based on state transition for cascaded H-bridge inverter under unbalanced DC sources," *IEEE J. Emerg. Sel. Top. Power Electron*., pp. 1686–1700, 2020.

[17] J. Kim, and Y. Cho, "Neutral voltage modulation for maximizing the linear modulation region and limp-home mode operation of multilevel cascaded inverters under DC-Link imbalance conditions," *IEEE Access* vol. 10, pp. 13515-13524, 2022.

[18] Z. Xia, Q. Wu, Z. Ye, D. Yu, L. Zhu, and W. Hu, "A Novel DC-Power Control Method for Cascaded Converter under DC Voltage-Imbalance Condition," *Journal of Electrical and Computer Engineering*, 2022.

[19] B. Xiao, L. Hang, J. Mei, C. Riley, L. M. Tolbert, and B. Ozpineci, "Modular cascaded h-bridge multilevel PV inverter with distributed MPPT for grid-connected applications," *IEEE Trans. Ind. Appl*., vol. 51, no. 2, pp. 1722–1731, 2015.

[20] Y. Yu, G. Konstantinou, C. D. Townsend, and V. G. Agelidis, "Comparison of zero-sequence injection methods in cascaded H-bridge multilevel converters for large-scale photovoltaic integration," *IET Renewable Power Gener.*, vol. 11, no. 5, pp. 603–613, May 2017.

[21] S. Rahimpour, O. Husev, D. Vinnikov, and V. N. Kurdkandi, H. Tarzamni, "Fault management techniques to enhance the reliability of power electronic converters: An overview," *IEEE Access*, vol. 11, pp. 13432–13446, 2023.

[22] O. Lopez, T. Komrska, J. Alvarez, and J. Adam, "Post-fault operation strategy for cascaded H-Bridge inverters driving a multi-phase motor," *IEEE Trans. Ind. Electron*., 2024, 71,5, 4309–4319.

[23] P. Lezana, and G. Ortiz, "Extended operation of cascade multicell converters under fault condition," *IEEE Trans. Ind. Electron*., vol. 56, pp. 2697–2703, 2009.

[24] W. Zhang, et al, "Survey on fault-tolerant techniques for power electronic converters," *IEEE Trans. Power Electron*. vol. 29, no. 12, pp. 6319–6331. 2014.

[25] P. W. Hammond, "Enhancing the reliability of modular medium-voltage drives," *IEEE Trans. Ind. Electron*., vol. 49, no. 5, pp. 948–954, 2002.

[26] F. Carnielutti, H. Pinheiro, and C. Rech, "Generalized carrier-based modulation strategy for cascaded multilevel converters operating under fault conditions," *IEEE Trans. Ind. Electron*., vol. 59, no. 2, pp. 679–689, 2012.

[27] M. Aleenejad, H. Mahmoudi, and R. Amhadi, "Unbalanced space vector modulation with fundamental phase shift compensation for faulty multilevel converters," *IEEE Trans. Power Electron*., vol. 31, no. 10, pp. 7225–7233, 2016.

[28] J. Lamb, B. Mirafzal, and F. Blaabjerg, "PWM common mode reference generation for maximizing the linear modulation region of CHB converters in islanded microgrids," *IEEE Trans. Ind. Electron.*, vol. 65, no. 7, pp. 5250–5259, Jul. 2018.

P. M. LINGOM, received the B.S. and M.S. degrees in Pedagogical Sciences and Electrical Engineering from ENSET, University of Douala, Cameroon, in 2014 and 2016, respectively. In 2022, he earned his PhD in Electrical Engineering, specializing in power and industrial electronics, from the Department of Electrical Engineering and Automation at Fuzhou University, China. From April 2022 to August 2023, he worked as a postgraduate intern at Opal-RT Technologies in Montreal, Canada. During this time, he contributed to developing new courseware in power electronics, motor drives, and renewable energy systems as part of a research collaboration with the University of Quebec at Trois-Rivieres (UQTR) under the Mitacs Canadian Program. Since October 2023, he has worked as a Postdoctoral Research Associate at Baylor

University. His research focuses on designing, fabricating, and testing power electronic converters based on wide-bandgap (WBG) semiconductors, emphasizing their associated control schemes for motor drives and renewable energy applications. He also actively engaged in real-time system modeling, simulation, and testing using Typhoon HIL, PLECS, and RTDS platforms.

Joseph SONG-MANGUELLE (M'07–SM'10) received the B.Sc. and M.Sc. degrees in pedagogical sciences and electrical engineering from ENSET, the University of Douala, Cameroon, in 1995 and 1997, respectively, and the Ph.D. degree in electrical engineering from the Swiss Federal Institute of Technology, Lausanne, Switzerland, in 2004. From 2004 to 2012, he held engineering positions with General Electric in Germany, France, and NY, USA, where he was involved in the development of torsional vibration control systems with VFDs and HVDC transmission and distribution systems for future long tieback subsea applications; he holds four patents and has published more than 50 papers. From 2012 to 2021, he was a Senior Electrical Engineer and VFD Subject Matter Expert for ExxonMobil in Texas, Russia, and Papua New Guinea, involved in technical qualification of high-power subsea electrical components, facilities design, commissioning, and troubleshooting. From 2021-2023, he joined the Oak Ridge National Laboratory, Knoxville, TN, USA, as a Distinguished R&D Staff, developing new high-power electronic research programs for the US National Transportation Research Center. Computer Sciences – Electronics – Automatic Control Since 2023, he has been with Shell Corporation as a Global Subject Matter Expert for large variable speed drive systems to accelerate the decarbonization of industry and transportation.

In parallel to his professional activities, since 2010, he has been co-supervising master's and Ph.D. students at the University of Douala, Fuzhou University, China, and the University of Quebec at Trois-Rivieres, QC, Canada, where he is an Adjunct Professor. Dr. Song-Manguelle was an Associate Editor for the IEEE Journal of Emerging and Selected Topics in Power Electronics.

Ideal Oscar LIBOUGA, received the B.Sc. degree in electrotechnics, electronics, and automatic control, the M.Sc degree in computer sciences, electronics, and automatic control, and the Ph.D. degree in electrical engineering and industrial control from the University of Ngaoundéré, Cameroon. From 2014 to 2015, he was a Lecturer, Department of Electrical and Computer Engineering, Catholic University Institute, Buea, Cameroon. From 2015 to 2023, he was a Lecturer, Department of Electrical and Power Engineering, Higher Technical Teachers' Training College of Kumba, University of Buea, Cameroon. Since 2023, he is a Senior Lecturer, Department of Electrical Engineering and Intelligent Systems, National Higher Polytechnic School of Douala, University of Douala, Cameroon, where also serves as deputy head of the Research Laboratory of Electronics, Electrotechnics, Automatic Control, and Telecommunications. His research interests include Signal & Image Processing, Data Science, Industrial Electronics, & Renewable Energy Systems.

Mamadou Lamine DOUMBIA (M'03) received the M.Sc. degree in electrical engineering from Moscow Power Engineering Institute (Technical University), Moscow, Russia, in 1989, the M.Sc. degree in industrial electronics from the Université du Québec à Trois-Rivières (UQTR), Trois-Rivieres, QC, Canada in 1994, and the Ph.D. degree in electrical engineering from the Ecole Polytechnique de Montreal, Montreal, QC, Canada, in 2000. From 2000 to 2002, he was a Lecturer at the Ecole Polytechnique de Montreal and the CEGEP Saint-Laurent, Montreal, QC, Canada. He was a Senior Research Engineer with the CANMET Energy Technology Centre, Natural Resources Canada (2002–2003) and a Researcher with the Hydrogen Research Institute (HRI) (2003–2005). Since 2005, he is a Professor with the Department of Electrical and Computer Engineering, UQTR. He has authored or co-authored more than 100 papers in international journals and conferences. His research interests include renewable energy systems, distributed energy resources, variable speed drives, power electronics, and power quality. Dr. Doumbia is a member of the IEEE Power Electronics Society and IEEE Communications Society. He is a Professional Engineer and a member of the Ordre des Ingenieurs du Quebec. He is currently an editorial board member of the International Journal of Renewable Energy Research and International Journal of Smart Grid.

Emmanuel B. Agamloh (S'02–M'05–SM'09) received the B.Sc. and M.Sc. degrees in electrical engineering from St. Petersburg State Technical University, St. Petersburg, Russia, in 1992 and 1994, respectively, and the Ph.D. degree in electrical and computer engineering from Oregon State University, Corvallis, OR, USA, in 2005. He is an Associate Professor with the Department of Electrical and Computer Engineering, Baylor University, Waco, TX, USA. His research interests include electric machine design, analysis, and testing, motor-drives and power electronics, with application areas in renewable energy, industrial, aerospace, transportation, and oil and gas. Dr. Agamloh received two IEEE First Prize Paper Awards for his research. His extensive industry experience includes a 14-year role as Technical Director of the Motors and Drives Laboratory at Advanced Energy Corporation in Raleigh, NC, USA. He was a Technical Paper Review Chair of the IEEE TRANSACTIONS ON INDUSTRY APPLICATIONS and a past Chair of the IEEE-IAS Electric Machines Committee. He was the General Chair of the 2022 IEEE Energy Conversion Congress and Exposition (ECCE) held in Detroit, Michigan.